Biomedical Signal Processing and Control 100 (2025) 106894

Contents lists available at ScienceDirect

Biomedical Signal Processing and Control

journal homepage: www.elsevier.com/locate/bspc

Honey Badger Aquila optimization-based deep learning with multi-kernel shape index histograms for diabetic macular edema classification

Shweta Reddy [a,*], Shridevi Soma [b]

[a] BLDEA's V.P. Dr. P.G. Halakatti College of Engineering, India
[b] Department of Computer Science & Engineering, Poojya Doddappa Appa College of Engineering, Kalaburagi, India

ARTICLE INFO

Keywords:
Diabetic Macular Edema (DME)
Honey Badger Algorithm (HBA)
Aquila Optimizer (AO)
Convolutional Neural Network (CNN)
Sailfish Optimizer (SFO)

ABSTRACT

Diabetic Macular Edema (DME) is the foremost reason for vision loss in patients having Diabetic Retinopathy (DR). In the earlier diagnosis of DR, Optical Coherence Tomography (OCT) plays a major part in detecting and classifying DR, thus preventing vision loss. Most people suffer from DME due to neglecting treatments, which may lead to blindness or visual impairment. If properly detected, this can be healed at an earlier phase. DME detection and classification is a challenging chore in affected patients. To vanquish the.

Challenging task, an effective method is proposed for DME detection as well as classification using the proposed Shape Index Histogram Honey Badger Aquila Optimization-based deep convolutional neural network (SIH+HBAO-based deep CNN). Pre-processing is conducted employing a Gaussian filter. After pre-processing, layer segmentation is conducted by Correlative-based gradient global thresholding with active contour. Then, feature extraction is performed whereas layer-specific features, texture features including Local Gradient Pattern (LGP) and proposed SIH with multi-kernel are extracted. Furthermore, the proposed SIH with multi-kernel feature is devised by modification of shape index histogram with multi-kernel. After that, DME detection and classification are conducted utilizing Deep CNN, which is tuned employing the proposed HBAO algorithm. The proposed HBAO algorithm is introduced by incorporation of Honey Badger Algorithm (HBA) and Aquila Optimizer (AO). Moreover, the proposed SIH+HBAO-based deep CNN attained maximal values of accuracy, sensitivity and specificity of 0.912, 0.913 and 0.917.

1. Introduction

Medical imaging is a complex resource of knowledge about patients and the data from imaging is a preliminary diagnostic tool in several cases of medical. OCT is the medical imaging modality that can be utilized in diverse medicinal fields [16], especially for diagnosing various diseases related to the eye. When compared to other techniques that utilize X-rays, OCT is safest as it applies a source of light, where radiations are not concerned and so it is also utilized for imaging of several characteristics of biological tissues [15,45]. Recently, OCT for 3-dimensional (3D) images assured to fill the identified gaps among larger fields of inspecting tissue to higher resolution of cellular tissue investigation with feasibility to go through tissue of about 2 mm deep [14]. It is stated as new imaging technology as it generates higher resolution cross-sectional images of the interior tiny structure of alive tissue [10,9]. The main reason for OCT fascinating the view of researchers and engineers in the field of photonics is the potential to become the first diagnostic imaging technology, where features of coherent optics are important. The optical sectioning capability of OCT enables the scanners of OCT to image the microscopic compositions in tissue at a depth afar the attainment of confocal microscopes and conventional bright-field [9]. OCT executes numerous longitudinal scans at a sequence of lateral positions to provide a 2-dimensional reflection site map in the sample [10]. Automatic diagnosis on OCT imaging is relatively novel and the majority of precedent tasks on analyzing OCT images have focused on issues of segmenting retinal layers [11]. Assessing the captured images [39,40] could be employed for earlier diagnosis of various diseases including DME by detecting the formation of normal and abnormal retina [21].

Macular edema is the bulging of the retina's macula or Muller cells, whereas the macula is the very sensible portion of the eye and it is responsible for sharp visualization. The affected patient experiences macula edema because of fluid accretion under the macula and this is the reason for the swelling and thickening of the macula [25]. DME is

* Corresponding author.
E-mail address: reddyshwetab@gmail.com (S. Reddy).

https://doi.org/10.1016/j.bspc.2024.106894
Received 8 July 2023; Received in revised form 30 March 2024; Accepted 7 September 2024
Available online 3 October 2024

the main reason for irreversible vision failure in each person having diabetes. It plays a vital part in preventing unfavourable consequences, like blindness [11]. The pathophysiology of DME is relatively difficult and not understood fully. Presently, several pharmacological composites are under examination for DR treatment [38,12]. DME can extend at any phase of DR but it happens more often as the interval of diabetes and amplification of DR ardor [13]. As DME can occur at any phase of DR [37], it is considered as main reason for loss of vision and a goal of novel therapies range [17]. It is caused by extreme vascular permeability that results in the thickening of the retina and the leaking of fluid as well as constituents of plasma [18]. Generally, DME patients are advised to treat using numerous focal laser photocoagulations for several months or years, which leads to a better option for protecting their vision, however, the patients should not anticipate an improvement in vision. The prediction is secured for patients who have considerable loss of vision due to DME. This offered higher motivation for developing novel treatments, despite this focal laser photocoagulation alone being confirmed for DME treatment. A main cause for poor advancement in developing novel treatments for DME is a lack of comprehension of its pathogenesis [19].

Based on pathogenic, DME is classified as a commonly tractional component, retino vascular component or tightly affixed posterior hyaloid component. Here in many cases, pathogenic components are joined, which results in a complex challenge for deciding the prevalent component and also the most revealed treatment. Clinical ophthalmoscopes with fluorescein angiography, bio-microscopic lenses and OCT are the most significant in assisting the detection of DME prevalent etiopathogenic components. DME happens during abnormal permeability of retinal capillaries that causes an inactive flow of blood or plasma into an extracellular space [20]. A decrease in the time and effort of ophthalmologists for diagnosing will be essential for lessening the expansion of DME cases. Deep learning [43,46,47] is rising as the foremost tool of machine learning in the computer aspect and is in progress for authorizing a major deliberation in the medical imaging field. Earlier detection utilizing deep learning techniques is mostly trustworthy for determining the occurrence of abnormalities in an image [22,21]. Recently, deep learning has demonstrated extraordinary performance in solving medical imaging issues and thus fascinated substantial concentration. Therefore, one of the characteristic chores is the detection of abnormalities and then classifying them into categories of disease [23,21]. Deep learning [48,49] techniques like CNN have quickly increased the importance of analyzation of medical images [4,41]. CNN has been demonstrated as a powerful tool for learning DME features [24,25,6]. CNN-based categorization strategies provide the best implementation due to their scale property, rotational property and expansive field of focus. In addition, CNN has a proficient enhancement for the recognition and characterization of images and it is consequently, implemented for frameworks of DR diagnosis [26].

The major intent of this research paper is to introduce an efficient detection and classification technique for DME based on the proposed SIH+HBAO-based deep CNN. Initially, the input image is considered from the particular database and after that pre-processing is performed utilizing a Gaussian filter. Thereafter, layer segmentation is done by Correlative-based gradient global thresholding with active contour, which is modified by including the adaptive concept into the gradient-based thresholding and global threshold into the active contour model and finally, the correlation coefficient is used for the fusion process. Afterwards, extraction of features is carried out in which layer-specific features including reflectivity, uniformity, thickness, variance, smoothness, and mean, as well as area and image level features like Fast Fourier Transform (FFT) and wavelet, are extracted. Additionally, texture features include LGP and proposed SIH with multi-kernel are extracted. The proposed SIH with multi-kernel feature is designed by modifying the shape index histogram with a multi-kernel. Lastly, DME detection and classification is carried out employing Deep CNN that is tuned utilizing the proposed HBAO algorithm. During detection, DME is detected into normal or abnormal cases, whereas in classification, the abnormal cases are further classified into diffuse retinal thickening, serous retinal detachment, cystoid macular, posterior hyaloid traction, and tractional retinal detachment categories utilizing Deep CNN that is trained using same proposed HBAO approach. The proposed HBAO algorithm is introduced by an integration of HBA [34] and AO [33].

The goal of this research is to classify patients with diabetic retinopathy and detect DME in those patients who have vision loss. Here, using the proposed Shape Index Histogram Honey Badger Aquila Optimization-based deep convolutional neural network (SIH+HBAO-based deep CNN). Pre-processing is conducted employing a Gaussian filter. After pre-processing, layer segmentation is conducted by Correlative-based gradient global thresholding with active contour. Then, feature extraction is performed whereas layer-specific features, texture features including Local Gradient Pattern (LGP) and proposed SIH with multi-kernel are extracted. Furthermore, the proposed SIH with multi-kernel feature is devised by modification of shape index histogram with multi-kernel.

The vital contribution of this probe paper is elucidated beneath:

- **Proposed SIH+HBAO-based deep CNN for Diabetic Macular Edema detection and classification:** The newly developed SIH+HBAO-based deep CNN technique is employed to predict DME. The devised SIH+HBAO is newly formed by the combination of HBA and AO. Here, SIH is proposed with multi-kernel to extract the features whereas DME detection and classification is conducted utilizing HBAO that is trained by deep CNN.

The rest of the portions in this research paper are ordered as follows: A literature overview of traditional techniques according to DME detection and classification is elucidated in section 2 and section 3 describes a proposed method for DME detection and classification. In section 4, the result of the proposed method is discussed and the conclusion is expounded in section 5.

2. Literature Review

Earlier detection and classification of DME are more significant and hence this portion illustrates the literature survey of eight research papers that applied classical techniques along with identified research gaps and challenges faced by these techniques are also described, which motivate the researchers for further development of new techniques related to DME detection and classification. This part elucidates literature reviews of current DME detection and classification techniques with merits and demerits. Harpal Singh Sandhu., *et al.* [1] developed a new computer-assisted diagnostic (CAD) model for detecting and classifying DR utilizing OCT images and a two-phase deep network was utilized for classifying normal, subclinical phase DR or moderate DR based on three discriminate features like curvature, reflectivity, and thickness. It automatically diagnosed non-proliferative diabetic retinopathy (NPDR) based on OCT images from type II diabetics is possible, trustworthy and precise but still it was not cooperated with OCT angiographic data for an enhancement of accuracy. Mohammed Ghazal., *et al.* [2] presented a new CAD system for earlier detection of DR-related alterations in OCT images utilizing CNNs. This method achieved maximal accuracy with minimum computational time. However, the scarcity of the data and the relative complexity of the problem. Xuechen Li., *et al.* [3] developed a new deep network– OCTD_Net for earlier phase classification of DR utilizing OCT images showing the probable of OCT images for detecting earlier phase DR in a cost and time-proficient manner but this method failed to add clinical history and other data sources for cross-modality earlier detection of DR. Rajeev Kumar Singh., *et al.* [4] developed DMENet algorithm utilizing Hierarchical Ensemble of CNNs (HE-CNN) for automatic DME screening. This technique has consistency over other current techniques on every metric that was most significant in the field of medicine whereas the possibility of a developed solution could not be

Table 1
Review of existing models.

Author	methods	Advantages	Disadvantages
Harpal Singh Sandhu., *et al.* [1]	CAD model utilizing OCT.	Automatically diagnosed non-proliferative diabetic retinopathy.	It was not cooperated with OCT angiographic data for an enhancement of accuracy.
Mohammed Ghazal., *et al.* [2]	CAD system using CNN.	This method achieved maximal accuracy with minimum computational time.	The scarcity of the data and the relative complexity of the problem.
Xuechen Li., *et al.* [3]	Deep network–OCTD_Net.	This method has a low cost and low response time.	This method failed to add clinical history and other data sources for cross-modality earlier detection of DR.
Rajeev Kumar Singh., *et al.* [4]	Diabetic macular edema Network (DMENet) algorithm.	This technique has consistency over other current techniques on every metric.	The possibility of a developed solution could not be tested in hospital settings.
Sivamurugan Vellakani., *et al.* [5]	Artificial intelligence (AI) based clinical decision support system.	Have a higher potential for ophthalmologists to make optimum diagnostic decisions.	This devised method did not utilise fused features for designing a novel training model for the generation of captions.
Xiaomeng Li., et al. [6]	Cross-disease attention network (CANet).	The better quality of the network over other methods on grading chores of DR and DME.	It failed to tune the network jointly with lesion annotations.
Akash Tayal., *et al.* [7]	Diagnostic tool based on a deep-learning framework.	This framework identified the harmful parameters affecting the algorithm's functions.	It did not consider the biological variations in the structure of the retina and eye.
Joaquim de Moura., *et al.* [8]	Fully automatic model.	This technique identified and segmented the pathological regions of each disorder of ME.	It did not automatically segment other diseases related to the eye.
Amit Kumar, *et al.* [42]	Densenet121.	The model serves to lessen the strain on ophthalmologists by diagnosing DME at an early stage so that it can be treated promptly.	Failed to work in the graphics processing unit (GPU) model.
Amit Kumar, *et al.* [44]	Squeeze-and-Excitation embedded densenet121 (SEDense).	This method reduces the hassle of ophthalmologists in diagnosing DME grades.	Required more memory to store intermediate feature maps.
Zeru Hai., *et al.* [51]	DRGCNN (DR Grading CNN) model.	This method provided better performance and established a highly competitive intelligent classification model.	Required large amounts of labeled data.

tested in hospital settings. Sivamurugan Vellakani., *et al.* [5] devised an artificial intelligence (AI) based clinical decision support system for the detection and classification of DME by OCT images that have higher potential for ophthalmologists in making optimum diagnostic decisions. This devised method did not utilise fused features for designing a novel training model for the generation of captions. Xiaomeng Li., *et al.* [6] presented a cross-disease attention network (CANet) for combinable grading of DR and DME and investigated the individual diseases demonstrating the better quality of the network over other methods on grading chores of DR and DME but still, it failed to tune the network jointly with lesion annotations. Akash Tayal., *et al.* [7] presented a diagnostic tool based on a deep-learning framework for the automatic detection of DME in OCT scans of the human eye. This framework identified the harmful parameters affecting the algorithm's functions but it did not consider the biological variations in the structure of the retina and eye. Joaquim de Moura., *et al.* [8] developed a fully automatic model for the detection, segmentation and classification of three kinds of ME utilizing OCT images that identified and segmented the pathological regions of each disorder of ME but this model did not automatically segment other diseases related to the eye. Amit Kumar., *et al.* [42] developed a method for detecting instances of DME from retinal fundus images using the idea of transfer learning. In this method, the fundus images are utilized to train a pre-trained DenseNet121 to extract the useful set of feature vectors, which are then passed into a few further fully connected layers and onto the classification layer to categorize DME occurrences. The model serves to lessen the strain on ophthalmologists by diagnosing DME at an early stage so that it can be treated promptly. However, it failed to work in the graphics processing unit (GPU) model. Amit Kumar., *et al.* [44] presented a technique for categorizing the severity of DME grades known as Squeeze-and-Excitation embedded DenseNet121 (SEDense). Pre-processing is carried out, including augmentation and green channel extraction. From the initial 413 images used for training, the augmentation creates 1170 images. It has a classification accuracy of 88.35 % for the DME grades. Ophthalmologists can diagnose DME grades with less effort thanks to the proposed SEDense model. This method reduces the hassle of ophthalmologists in diagnosing DME grades. Yet, it required more memory to store intermediate feature maps. Zeru Hai., *et al.* [51] proposed the Diabetic Retinopathy Grading Convolutional Neural Networks (DRGCNN) model for the diagnosis of diabetic retinopathy. This method provided better performance and established a highly competitive intelligent classification model. However, it required a large amount of labeled data. Table 1 shows a Review of existing models.

3. Proposed SIH+HBAO-Based deep CNN for Diabetic Macular edema detection and classification

DME happens at any phase of proliferative and non-proliferative DR, which leads to worsening of vision. Therefore, earlier detection and classification are very important for DME to protect the vision. Hence, an efficient technique is proposed employing SIH+HBAO-based deep CNN. Firstly, the input image is considered from a particular database specified in [35] and then pre-processing is carried out employing a Gaussian filter. Afterwards, layer segmentation is performed by Correlative-based gradient global thresholding with an active contour that is modified by including an adaptive concept into the gradient-based thresholding and global threshold into an active contour model and then, the correlation coefficient is utilized for the fusion process. Thereafter, feature extraction is done whereas layer-specific features, texture features including LGP and proposed SIH with multi-kernel are extracted. Moreover, the proposed SIH with the multi-kernel feature is introduced by modifying the shape index histogram with multi-kernel. Finally, DME detection and classification are performed employing Deep CNN that is tuned utilizing the proposed HBAO algorithm. The proposed HBAO algorithm is introduced by an integration of HBA [34] and AO [33]. During detection, DME is detected into normal or abnormal cases whereas, in classification, the abnormal cases are further classified into diffuse retinal thickening, serous retinal detachment, cystoid macular, posterior hyloid traction, and tractional retinal detachment categories. Fig. 1 explicates the diagrammatic view of the proposed SIH+HBAO-based deep CNN for the detection and classification of DME.

Acquisition of input image

Consider the OCT image for DME as an input image that is acquired

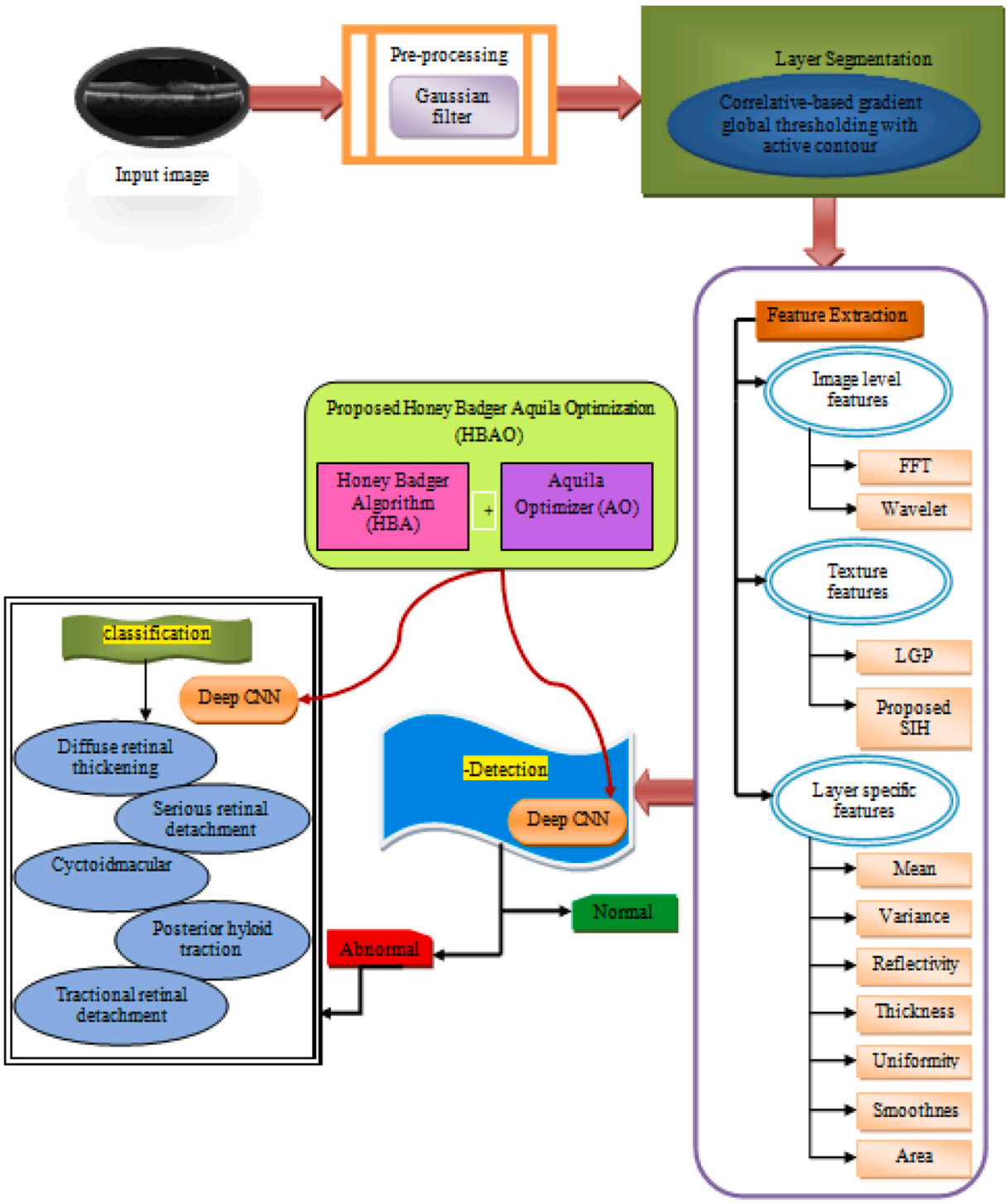

Fig. 1. Diagrammatic view of proposed SIH+HBAO-based deep CNN for DME detection and classification.

from a particular database mentioned in [35] and it is represented as given below,

$$Z = \{I_1, I_2, \ldots I_d \ldots I_m\} \tag{1}$$

Here, m represents the overall number of training images in the training database Z, whereas I_d implies d^{th} input image.

3.1. Pre-Processing utilizing Gaussian filtering

Image pre-processing is the initial stage in several feature description techniques. It is utilized for eliminating unnecessary alterations and noises that enhance the quality of the image. In this phase, Gaussian filtering [27] is used to suppress the noise and also, the noise is smoothed out. The one-dimensional Gaussian filter can be formulated by,

$$F(p) = \frac{1}{\sqrt{2\Pi\sigma}} \exp\left(-p^2/2\sigma^2\right) \tag{2}$$

Here, σ^2 denotes the variance of Gaussian filter whereas two-dimensional Gaussian filter is represented by,

$$F(p,q)=\frac{1}{\sqrt{2\Pi\sigma}}\exp\left(-\left(p^2+q^2\right)/2\sigma^2\right) \tag{3}$$

Where, p and q signifies the distance from the origin to the vertical axis and horizontal axis. Therefore, the pre-processed outcome G_d is the input for the layer segmentation process.

3.2. Layer segmentation using Correlative-Based gradient global thresholding with active contour

After pre-processing is commenced, layer segmentation is performed for segmenting the layers in images. Here, layer segmentation is performed utilizing correlative-based gradient global thresholding with active contour, which is modified by including an adaptive concept into the gradient-based thresholding and global threshold into an active contour model and thereafter, the correlation coefficient is employed for the fusion process.

3.2.1. Active global contour model

A resultant image from the prior phase G_d is taken for the active contour model in the layer segmentation stage, where segmentation of retinal areas is performed. An active contour model mostly depends on an energy minimization technique that takes account of interior and exterior forces. It persistently drags the contour for moving in the direction of image features and it is formulated by,

$$A_s=\int_{c=0}^{1}A_{\text{int}}^{s}\left(\mu_c(c)^2\right)+A_{ext}^{s}\left(\mu_{cc}(c)^2\right)dc \tag{4}$$

Here, the internal energy is indicated by A_{int} and is described as the functional term of the first order $\mu_c(c)^2$, which reveals the elasticity evaluation and the functional term of the second order is $\mu_{cc}(c)^2$ that denotes the active contour collecting the thin plate behavior, which signifies the curvature. Thereafter, functional terms of first as well as second order are operated using invariable weight factors like, φ and ϕ. In addition, an expression of internal energy is represented as,

$$A_{\text{int}}^{s}=\frac{1}{2}\left(\varphi|\mu_c(c)|^2\right)+\frac{1}{2}\left(\phi|\mu_{cc}(c)|^2\right) \tag{5}$$

External energy is used for pulling a contour model by the intensity behaviour of an image G_d, which is given as,

$$A_{ext}^{s}=-|\nabla G_d(c)|^2 \tag{6}$$

Here, ∇G_d denotes an image gradient. An output obtained from the active contour model is V_d.

3.2.2. Gradient-based adaptive thresholding

In this method, the retinal regions are altered to several layers whereas the gradient-based adaptive thresholding [28] is carried out utilizing gradient-based threshold values of OCT image and it is indicated by T_d. Initially, OCT image gradient values are evaluated and thereafter extraction of upper and lower retinal layers is carried out. Thereafter, binary mask layers are generated and then, retinal sections are separated by multiplying binary mask along with an input image, Afterwards adaptive thresholding method is passed to regions for segmentation of fluid portion from the retina.

Additionally, DME portions from the retina are founded by incorporation of gradient-based adaptive thresholding method output T_d and output obtained in active contour method V_d and it is formulated by,

$$S_d=\varepsilon V_d+\tau T_d \tag{7}$$

Here, ε and τ denotes the random number that ranges between 0 and 1.

Here, the thresholding value is selected as follows [29]: Initially, select an input estimation for H and then, segment the image utilizing H which generates two-pixel groups whereas R_1 comprising of pixels with grey level values $< H$ and R_2 comprising of pixels $\leq H$. Afterwards, calculate the mean grey level values M_1 and M_2 for pixels in R_1 and R_2. Thereafter, calculate a new threshold value by using the below Eq. (8). Repeat the steps until the difference H for consecutive iteration is minimum than a pre-defined parameter H_0.

$$H=\frac{1}{2}(M_1+M_2) \tag{8}$$

Therefore, the output of adaptive thresholding is signified by S_d.

3.2.3. Fusion based on correlation coefficient

A correlation coefficient is a definite measure that quantifies the linear relationship strength among two variables. Here, the output of an active global contour model V_d and output of gradient-based adaptive thresholding S_d are fused utilizing correlation coefficient and output for layer segmentation is signified by L_d, where

$$L_d=\begin{cases}V_d & \text{if } C(V_d,S_d)=1\\ \textit{Majority voting based solution} & \text{if } C(V_d,S_d)\neq 1\end{cases} \tag{9}$$

If the correlation coefficient,C of outputs V_d,S_d is not equal, then take the neighboring pixels of segmented outputs V_d as well as S_d select the majority pixel number based upon voting.

3.3. Feature extraction

Feature extraction is a method where an image having a large number of pixels is proficiently represented in such a way that fascinating parts of an image are captured efficiently. Here, L_d is considered as an input and image level features, texture features as well as layer specific features are extracted from L_d.

3.3.1. Image level features

Firstly, extractions of image-level features from segmented layers are carried out by involving FFT as well as wavelet coefficients.

(i) FFT: Here, features of the retina are extracted based on a periodic function with FFT, which is represented below,

$$E_1=\sum_{-\infty}^{\infty}\lambda_f.e^{(-2a\pi J/K)} \tag{10}$$

Here, K indicates the total of boundary points and the time is denoted by J. Fourier coefficients are signified by λ_f and it is formulated as,

$$\lambda_f=\frac{1}{K}\int_0^K l_2(J).e^{(-2a\pi aJ)}dJ \tag{11}$$

Where, l_2 implies an extracted image level feature from the segmented output. E_1 denotes the FFT feature.

(ii) Wavelet coefficient feature: A wavelet is a wave-like oscillation having an amplitude that starts at zero, maximizes or minimizes and thereafter returns to zero one or numerous times. The wavelet feature is expressed by,

$$E_2=\frac{1}{\xi}\delta\left(\frac{\nu-w}{\xi}\right) \tag{12}$$

Here, the scaling factor is indicated by ξ, w denotes a shifting factor, ν signifies a real integer and a wavelet feature is represented by E_2.

3.3.2. Texture feature

Texture is a vital part of human visual perception and it is utilized in several computer vision methods. Here, LGP and proposed SIH are considered for the extraction of texture features.

(i) LGP: LGP is a fundamental and intrinsic property of human visual perception, which is generally utilized for characterizing the several local semantic frameworks of an image. An expression of LGP is given by,

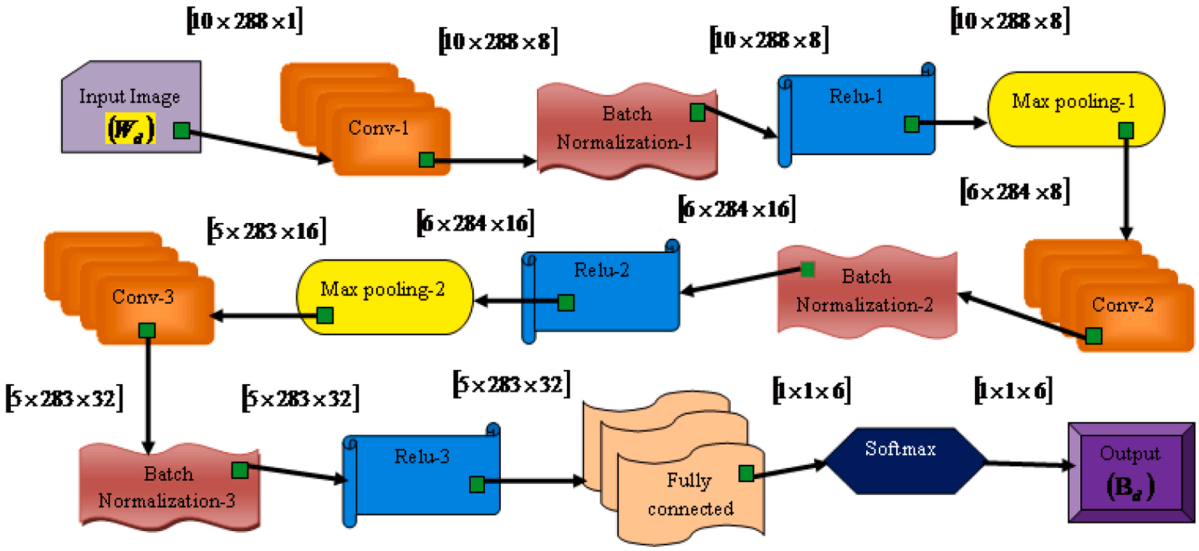

Fig. 2. The architecture of Deep CNN.

$$P_{u,v}(x_r, y_r) = \sum_{z=0}^{n} I(D_z - \overline{D})\, 2^z \tag{13}$$

Here, $P_{u,v}(x_r, y_r)$ this signifies the LGP feature at the center pixel location (x_r, y_r), u and v are radius and gradient values. An average set of v gradient values is formulated by, $\overline{F} = \left(\frac{1}{v}\right) \sum_{z=0}^{n} D_z$. LGP feature is indicated by E_3.

(ii) Proposed SIH.

The SI captures the structure of 2nd order image in an incessant period that permits to overview of the distributions of curvature in a histogram [32].

By applying linear kernel in Gaussian aperture function, the equation is expressed as,

$$\kappa_1(b, \lambda) = g^R g + \mathrm{Z} \tag{14}$$

Here, λ denotes the width of the Gaussian kernel and b indicates the spatial coordinates.

Then, by applying a sigmoid kernel in the Gaussian aperture function, the equation is formulated by,

$$\kappa_2(b, \lambda) = \tanh\left(\gamma . g^R g + i\right) \tag{15}$$

Thereafter, applying polynomial kernel in Gaussian aperture function, the equation is given by,

$$\kappa_3(b, \lambda) = \left(\beta g^R g + \mathrm{Z}\right)^j \tag{16}$$

Where, Z and β are constants. Therefore, the modified equation obtained for the proposed SIH is mentioned as multi kernel equation, which can be formulated as,

$$\kappa(b, \lambda) = \frac{\kappa_1(b, \lambda) + \kappa_2(b, \lambda) + \kappa_3(b, \lambda)}{3} \tag{17}$$

An output of the proposed SIH feature is denoted by E_4 .

Thus, an extracted image is given by,

$$X_d = \{E_1, E_2, E_3, E_4\} \tag{18}$$

3.3.3. Layer specific features

Here, the features like reflectivity, thickness, uniformity, smoothness, mean, variance and area are extracted.

(i) Reflectivity: This feature is utilized for extracting two segments like the thickest portion of the retina and it is denoted by k_1.

(ii) Thickness: The distance between an upper and lower retinal surface and it is indicated by k_2.

$$\nabla^2 \varsigma = \frac{\partial^2 \varsigma}{\partial \mathrm{O}_t^2} + \frac{\partial^2 \varsigma}{\partial \mathrm{K}_t^2} \tag{19}$$

Here, $\varsigma(\mathrm{O}_t, \mathrm{K}_t)$ are known as harmonic functions.

(iii) Uniformity: Uniformity is defined as a maximal value reached when all the intensities are equal. It is signified by k_3.

(iv) Smoothness: This feature decreases the noises or produces a low pixilated image and it is revealed by k_4.

(v) Mean: Mean value is the total pixel values divided by the overall count of pixel values whereas mean is represented by k_5.

$$k_5 = \frac{1}{m_e} \sum_{d=1}^{m} L_d \tag{20}$$

Here, m indicates the total amount of images and output segmented layer is denoted by L_d .

(vi) Variance: It is a square of the standard deviations in the values of input or output images and the variance is expressed by k_6.

$$k_6 = \frac{1}{m_e} \sum_{d=1}^{m} (L_d - k_5) \tag{21}$$

Where, k_5 indicates the mean.

(vii) Area: The area of an image is defined as a space enclosed within the perimeter or the boundary of a given image and it is denoted by k_7.

Then, layer-specific features are applied to each extracted image and hence the expression is given as follows.

$$W_1 = \{k_1, k_2, k_3, k_4, k_5, k_6, k_7\} \tag{22}$$

$$W_2 = \{k_1, k_2, k_3, k_4, k_5, k_6, k_7\} \tag{23}$$

$$W_3 = \{k_1, k_2, k_3, k_4, k_5, k_6, k_7\} \tag{24}$$

$$W_4 = \{k_1, k_2, k_3, k_4, k_5, k_6, k_7\} \tag{25}$$

Therefore, the feature vector output is represented by,

$$W_d = \{W_1, W_2, W_3, W_4\} \tag{26}$$

3.4. DME detection using proposed HBAO-Based deep CNN

Detection of DME is performed by the proposed HBAO, which is trained by deep CNN. A major purpose of utilizing deep CNN is that it offers efficient detection and classification. Here, detection of DME is

Table 2
Experimental parameters.

Parameters	Deep NN	CNN	OCTD-Net	G-AT-AC+ALSMO-GAN	SEDense	Akash Tayal., *et al*	HE-CNN	3D-CNN	Proposed SIH+HBA O-based deep CNN
Epoch	100	100	100	100	100	100	100	100	100
Batch size	32	64	32	32	32	32	32	32	64
Learning rate	0.01	0.01	0.01	0.01	0.01	0.01	0.01	0.01	0.01
Convolutional layers	3	3	3	3	3	3	3	3	4
Pooling layers	3	3	3	3	3	3	3	3	4
Optimizer	adam	adam	adam	adam	adam	adam	adam	adam	adam

Table 3
Disease Types.

Type of Disease	Total images
CMD	287
DRT	73
PHT	21
SRD	28
TRD	28

carried out, which results in normal or abnormal.

3.4.1. Architecture of deep CNN

CNN is a sort of artificial neural network that involves a convolutional layer along with non-linear, fully connected and pooling layers to form a deep CNN [36]. Deep CNN architecture is delineated in Fig. 2. The layer types of Deep CNN are described below.

Convolutional layers: Here, plentiful filters glide over a layer for particular input data. After that, an evaluation of the output layer is carried out by summation of element-by-element multiplication of filters as well as the receptive field of an input. It is formulated as,

$$\left(\mathrm{AB}_o^{qq}\right)_{\hbar,\lambda} = \left(Q_o^{qq}\right)_{\hbar,\lambda} + \sum_{\vartheta=1}^{\omega_1^{\vartheta-1}} \sum_{\chi=\omega_1^{qq}}^{\omega_1^{qq}} \sum_{\varpi=-\omega_2^{qq}}^{\omega_2^{qq}} \left(\Psi_{0,\vartheta}^{qq}\right)_{\varpi,\chi} * \left(AB_d^{qq-1}\right)_{\hbar+\chi,\lambda+\varpi} \quad (27)$$

In the above equation, a permanent feature map or output of qq^{th} convolutional layer, which is centered as $(\hbar,\lambda)$ is represented by $\left(\mathrm{AB}_o^{qq}\right)_{\hbar,\lambda}$. The weight and bias of qq^{th} the convolutional layer are $\Psi_{0,\vartheta}^{qq}$ and Q_o^{qq}. An output of the previous $(qq-1)^{th}$ layer develops the input to mm^{th} the convolutional layer and a convolutional operator is denoted by $*$. Likewise, ϑ,χ and ϖ indicates the feature maps, which perform as an output of each convolutional layer.

Pooling Layer: This layer diminishes the dimension of an input although, it is non-parametric and performs stable operations.

Fully connected layers: The data from the pooling layer is thereafter fed to the fully connected layer. This layer operates as the classifier and it is significant to train non-linear incorporation of characteristics. An output obtained from deep CNN is signified by B_d. The fully connected expression is given by,

$$FC_o^{qq} = \Omega\left(AB_o^{qq}\right) \quad \text{with} \quad \sum_{\vartheta=1}^{\omega_1^{\vartheta-1}} \sum_{\chi=\omega_1^{qq}}^{\omega_1^{qq}} \sum_{\varpi=-\omega_2^{qq}}^{\omega_2^{qq}} \left(\Psi_{0,\vartheta}^{qq}\right)_{\varpi,\chi} \left(AB_d^{qq-1}\right)_{\hbar+\chi,\lambda+\varpi} \quad (28)$$

Aquila position encoding

To attain the optimum solution in a search space, the learning parameter is trained until achieving the optimal solution, in which the learning parameter is indicated ℓ.

Fitness function

The difference between destination output and achieved output from the deep CNN is known as fitness function and it is illustrated by,

$$FF = \frac{1}{m} \sum_{d=1}^{m} \left[Tg_d - \mathrm{B}_d\right]^2 \quad (29)$$

Where the total number of samples is signified by m, destination output and outputs attained from deep CNN are represented by Tg_d and B_d, respectively.

3.4.2. Training of deep CNN utilizing proposed HBAO

HBA solves difficult problems of optimization with various local areas as well as it has better convergence speed and balancing of exploration and exploitation phases. AO performs the hunting action of Aquila at every step. Initially, the search space is selected and explored within a diverging space whereas exploitation occurs within a converging space and then finds the optimum solution. Hence, deep CNN is tuned for effectual operations, employing the proposed HBAO.

Step 1: Solution Initialization

AO is a population-based optimization approach in which a tenet for optimization initializes with a candidate solution population (H) in a search space $m_m \times n_n$ as revealed in Eq. (30). A supreme solution is considered as an optimal solution in all iteration, which is illustrated by,

$$\mathrm{H} = \{\mathrm{H}_1, \mathrm{H}_2, \ldots\ldots\ldots, \mathrm{H}_d, \ldots\ldots \mathrm{H}_o\} \quad (30)$$

Here, an existing candidate solution, which is generated randomly by Eq. (28), the location of d^{th} the solution is represented by H_d, the overall candidate solution population is indicated by o and the problem dimension is presented by m_n. It is given as,

$$\mathrm{H}_{dff} = rand \times \left(UU_{ff} - LL_{ff}\right) + LL_{ff}, \quad d = 1, 2, 3\ldots\ldots\ldots o \;\; ff - 1, 2, 3, \ldots\ldots\ldots\ldots m_n \quad (31)$$

Here, a random number is signified by *rand* UU_{ff} and LL_{ff} implies ff^{th} the upper and the lower bound of the known problem.

Step 2: Evaluate Objective Function

Here, a difference between targeted output and obtained output from deep CNN is evaluated utilizing Eq. (29).

Step 3: Expanded Exploration (H_1).

Here, an Aquila identifies the prey region and elects the finest region for haunting by higher ascent with vertically bending down. Hence, AO broadly identifies the region of search space having the prey from higher ascent. The expression is represented below.

$$\mathrm{H}_1(e+1) = \mathrm{H}_{best}(e) \times \left(1 - \frac{e}{N}\right) + \left(\mathrm{H}_{\mathrm{M}}(e) - \mathrm{H}_{best}(e) * rand\right) \quad (32)$$

Here, $\mathrm{H}_1(e+1)$ is the next iteration solution e that is created by the first search method (H_1). $\mathrm{H}_{best}(e)$ is an obtained finest solution until e^{th} iteration, which shows the position of prey. The equation $\left(1 - \frac{e}{N}\right)$ is utilized for controlling the expanded or exploration search concerning the count of iterations. The mean value position of present solutions is indicated by $\mathrm{H}_{\mathrm{M}}(e)$. Random value is signified by *rand* and the value ranges between 0 and 1. Maximal iteration and present iteration are implied by N and e. The equation (29) is then simplified as follows,

$$\mathrm{H}_1(e+1) = \mathrm{H}_{best}(e) \left[\left(1 - \frac{e}{N}\right) - rand\right] + \mathrm{H}_{\mathrm{M}}(e) \quad (33)$$

Where,

$$\mathrm{H}_{\mathrm{M}}(e) = \frac{1}{o} \sum_{d=1}^{o} \mathrm{H}_d(e) \quad (34)$$

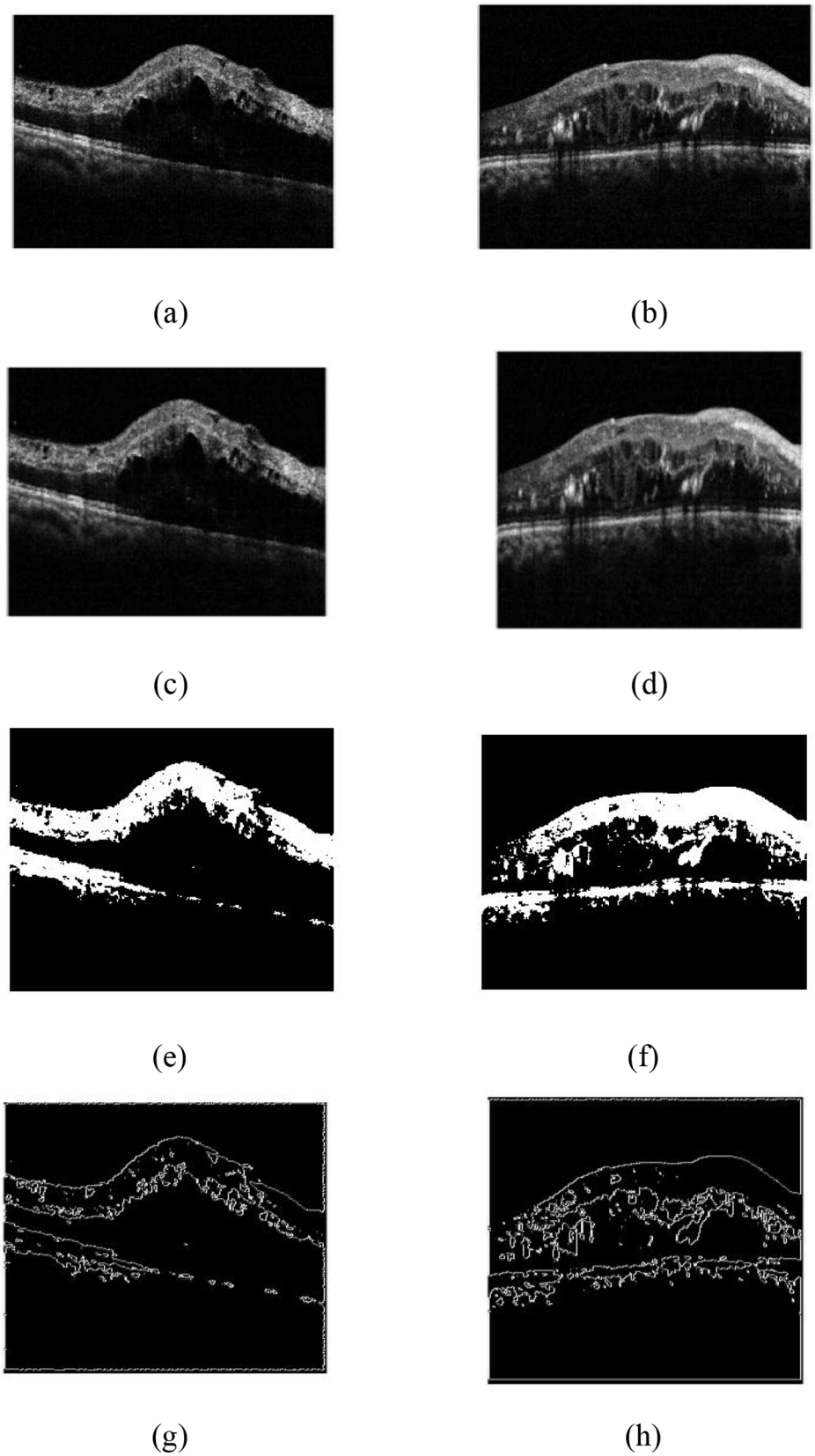

Fig. 3. Experimentation outcomes of (a) input image-1, (b) input image-2, (c) filtered image-1, (d) filtered image-2, (e) segmented image-1, (f) segmented image-2, (g) extracted image-1 of LGP feature, (h) extracted image-2 of LGP feature.

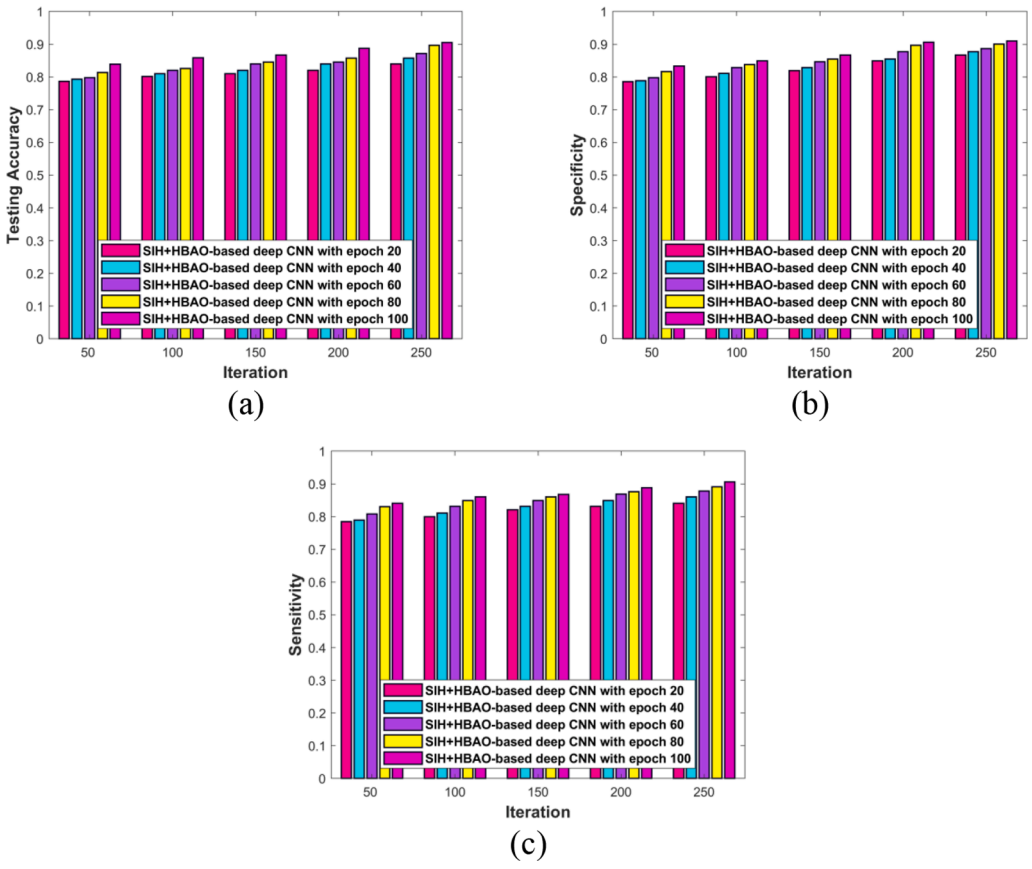

Fig. 4. Assessment based upon 1st level classification (a) Testing accuracy, (b) Specificity, (c) Sensitivity.

$$\frac{1}{o}\sum_{d=1}^{o} \mathrm{H}_d(e) = \mathrm{H}_1(e) \tag{35}$$

Then assume, $o = 1$ so the equation becomes,

$$\mathrm{H}_1(e+1) = \mathrm{H}_{best}(e)\left[\left(1-\frac{e}{N}\right) - rand\right] + \mathrm{H}_1(e) \tag{36}$$

The above equation is an updated equation of AO. Then, from honey badger,

$$\mathrm{H}_{1new} = \mathrm{H}_{1prey} + \mathrm{E} \times rn_7 \times \mathrm{T} \times dis \tag{37}$$

The above equation H_{1new} denotes a honey badger's new position and H_{1prey} signifies the location of prey. E indicates the disturbance and T is the time variation. rn_7 is the random number ranging between 0 and 1. The location of prey is identified based on distance information *dis* where,

$$dis = \mathrm{H}_{1prey} - \mathrm{P}_d \tag{38}$$

Then, the equation becomes,

$$\mathrm{H}_{1new} = \mathrm{H}_{1prey} + \mathrm{E} \times rn_7 \times \mathrm{T} \times \left(\mathrm{H}_{1prey} - \mathrm{P}_d\right) \tag{39}$$

$$\mathrm{H}_{1new} = \mathrm{H}_{1prey}(1 + \mathrm{E} \times rn_7 \times \mathrm{T}) - \mathrm{E} \times rn_7 \times \mathrm{T} \times \mathrm{P}_d \tag{40}$$

$$\text{Let, } \mathrm{H}_{1new} = \mathrm{H}_1(e+1) \tag{41}$$

$$\mathrm{H}_{1prey} = \mathrm{H}_{1prey}(e) \tag{42}$$

$$\mathrm{P}_d = \mathrm{H}_1(e) \tag{43}$$

Therefore, equation (37) becomes,

$$\mathrm{H}_1(e+1) = \mathrm{H}_{1prey}(e)\,(1 + \mathrm{E} \times rn_7 \times \mathrm{T}) - \mathrm{E} \times rn_7 \times \mathrm{T} \times \mathrm{H}_1(e) \tag{44}$$

$$\mathrm{H}_1(e) = \frac{\mathrm{H}_1(e+1) - \mathrm{H}_{1prey}(e)\,(1 + \mathrm{E} \times rn_7 \times \mathrm{T})}{\mathrm{E} \times rn_7 \times \mathrm{T}} \tag{45}$$

$$\mathrm{H}_1(e) = \frac{\mathrm{H}_{1prey}(e)\,(1 + \mathrm{E} \times rand \times \mathrm{T}) - \mathrm{H}_1(e+1)}{\mathrm{E} \times rand \times \mathrm{T}} \tag{46}$$

Substitute equation (43) in (33),

$$\mathrm{H}_1(e+1) = \mathrm{H}_{best}(e)\left[\left(1-\frac{e}{N}\right) - rand\right] + \left[\frac{\mathrm{H}_{1prey}(e)\,(1 + \mathrm{E} \times rn_7 \times \mathrm{T}) - \mathrm{H}_1(e+1)}{\mathrm{E} \times rn_7 \times \mathrm{T}}\right] \tag{47}$$

$$\mathrm{H}_1(e+1) + \frac{\mathrm{H}_1(e+1)}{\mathrm{E} \times rn_7 \times \mathrm{T}} = \mathrm{H}_{best}(e)\left[\left(1-\frac{e}{N}\right) - rand\right] + \left[\frac{\mathrm{H}_{1prey}(e)\,(1 + \mathrm{E} \times rn \times \mathrm{T})}{\mathrm{E} \times rn_7 \times \mathrm{T}}\right] \tag{48}$$

$$\mathrm{H}_1(e+1) + \frac{(\mathrm{E} \times rand \times \mathrm{T} + 1)}{\mathrm{E} \times rand \times \mathrm{T}} = \mathrm{H}_{best}(e)\left[\left(1-\frac{e}{N}\right) - rand\right] + \left[\frac{\mathrm{H}_{1prey}(e)\,(1 + \mathrm{E} \times rand \times \mathrm{T})}{\mathrm{E} \times rand \times \mathrm{T}}\right] \tag{49}$$

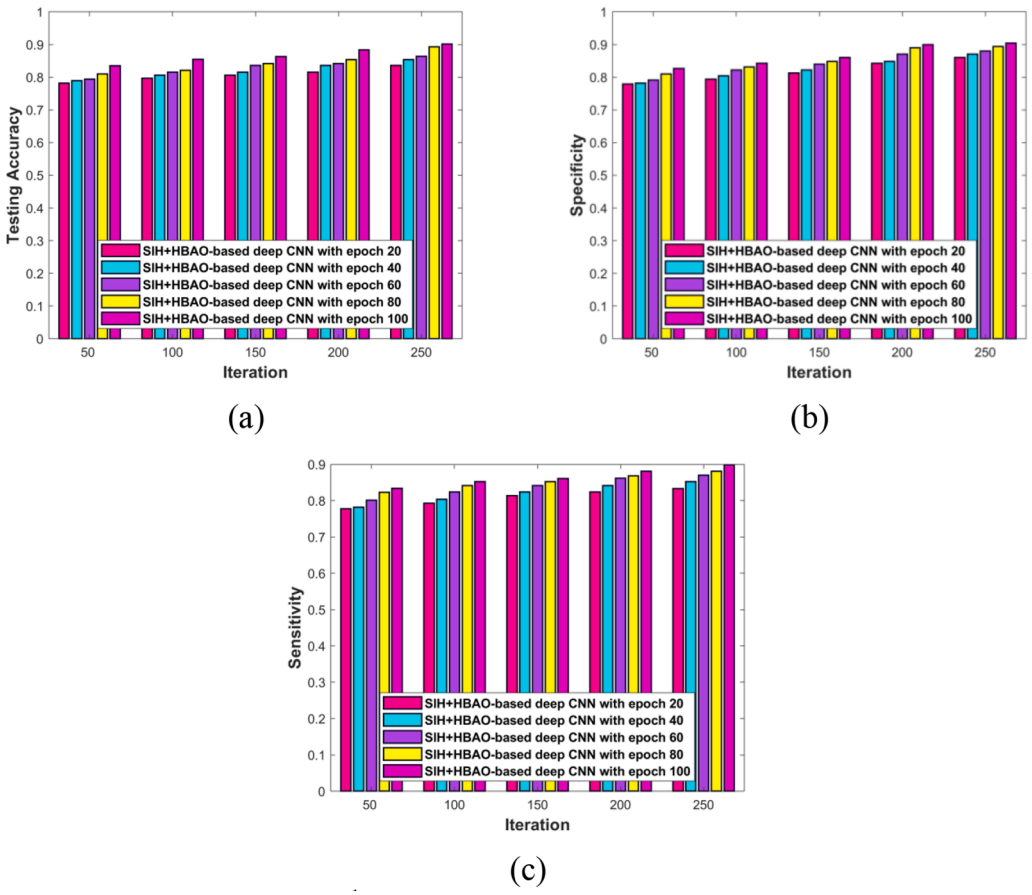

Fig. 5. Analysis based on 2nd level classification (a) Testing accuracy, (b) Specificity, (c) Sensitivity.

$$H_1(e+1) = \left[\frac{E \times rn_7 \times T}{(E \times rn_7 \times T + 1)}\right] \left[\frac{(E \times rn_7 \times T)H_{best}(e)\left[\left(1 - \frac{e}{N}\right) - rand\right] + H_{1prey}(e)\,(1 + E \times rn_7 \times T + 1)}{E \times rn_7 \times T}\right] \tag{50}$$

The final update equation of HBAO is given by,

$$H_1(e+1) = \frac{(E \times rn_7 \times T)H_{best}(e)\left[\left(1 - \frac{e}{N}\right) - rand\right] + H_{1prey}(e)\,(1 + E \times rn_7 \times T + 1)}{(E \times rn_7 \times T + 1)} \tag{51}$$

$$\text{Here, } E = \begin{cases} 1 & if\ rn_6 \le 0.5 \\ -1 & else \end{cases} \tag{52}$$

$$T = C_t \times \exp\left(\frac{-e}{e_{\max}}\right) \tag{53}$$

Here, $e_{\max}$ signifies a maximal count of iterations and C_t is constant, where $C_t \ge 1$. The randomly selected number is denoted by rn_6.

Step 4: Narrowed Exploration (H_2).

In the secondary method.

(H_2), an Aquila identifies the prey region from higher soar and circques above the targeted prey, and then it arranges the land and assaults the prey. Here, the chosen region for targeted prey is identified by AO and then prepared for an assault. The expression is illustrated by,

$$H_2(e+1) = H_{best}(e) \times Levy(\Upsilon) + H_{\Re}(e) + (r_r - s_s)^{*}rand \tag{54}$$

Here, $H_2(e+1)$ is a solution of successive iteration e that is obtained by H_2, dimensional space and levy flight distribution function is signified by Υ and $Levy(\Upsilon)$, which is computed by Eq. (52). Randomly chosen solution in a range among $[1 \;\; o]$ at the d^{th} iteration is implied by $H_{\Re}(e)$.

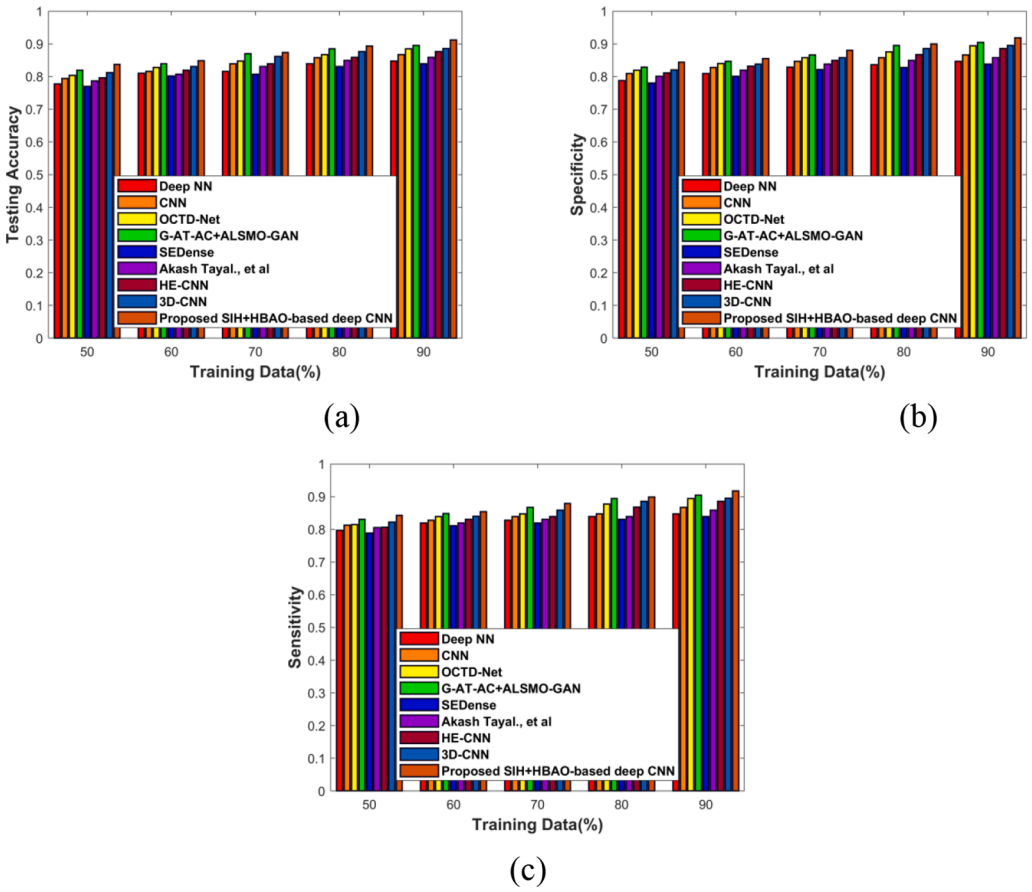

Fig. 6. Analysis based upon 1st level classification a) Testing accuracy, b) Specificity, c) Sensitivity.

$$Levy(\Upsilon) = t_c \times \frac{p_1 \times \mu_n}{|q_1|^{\frac{1}{\gamma_c}}} \tag{55}$$

Where, t_c is the constant value set to 0.01 whereas p_1 and q_1 are the random numbers among 0 and 1. μ_n is computed by the following expression,

$$\mu_n = \frac{\rho_a(1+\gamma_c) \times \sin e\left(\frac{\pi\gamma_c}{2}\right)}{\rho_a\left(\frac{(1+\gamma_c)}{2}\right) \times \gamma_c \times 2^{\left(\frac{\gamma_c-1}{2}\right)}} \tag{56}$$

Here, γ_c is constant value set to 1.5. Equation (51), r_r and s_s are utilized to represent a spiral formation in search that is formulated as below,

$$r_r = z_e \times \cos(\theta) \tag{57}$$

$$s_s = z_e \times \sin(\theta) \tag{58}$$

Where,

$$z_e = z_{e1} + W_b \times D_i \tag{59}$$

$$\theta = \varpi_h \times D_i + \theta_1 \tag{60}$$

$$\theta_1 = \frac{3 \times \pi}{2} \tag{61}$$

Here, z_{e1} the value ranges from 1 to 20 for the invariable count of search cycles and W_b is the least value that is set to 0.00565. D_i is the integer from 1 to search spacious dimension m_n and ϖ_h is the least value fixed to 0.005.

Step 5: Expanded Exploitation (H_3).

In (H_3), after the prey region is founded exactly, Aquila prepares for alighting and then assaults. The Aquila drops in a vertical manner having prime assault. Here, AO utilizes the chosen targeted region to move closer to prêt and assaults. It is represented by,

$$H_3(e+1) = (H_{best}(e) - H_M(e)) \times \alpha_p - rand + ((UU - LL) \times rand + LL) \times \partial_p \tag{62}$$

Here, $H_3(e+1)$ is the successive iteration solution e that is obtained by (H_3), $H_{best}(e)$ represents an approximative position of prey up to d^{th} iteration best solution is attained and $H_M(e)$ signifies the current solution mean at d^{th} iteration, *rand* is randomly selected value among 0 and 1. Exploitation adjustment parameters are denoted by α_p and ∂_p that is set to least value 0 and 1 *UU* and *LL* indicates upper and lower bound of a known problem.

Step 6: Narrowed Exploitation (H_4).

In the fourth method (H_4) , the Aquila moves about nearer to prey and then assaults prey above the land in accordance with speculative motions. Here, AO assaults a prey in the last location. It is mathematically represented as,

$$H_4(e+1) = Q_f \times H_{best}(e) - (\Im_1 H(e) \times rand) - \Im_2 Levy(\Upsilon) + rand \times \Im_1 \tag{63}$$

Here, $H_4(e+1)$ is a successive iteration solution e that is formed by (H_4). Q_f represents a quality function, which is utilized to balance the search plans. Several movements of AO are signified by $\Im_1$ whereas $\Im_2$ is the flight slope of AO. $\Im_1$ is used for tracking the prey, which is achieved by equation (62) and $\Im_2$ is utilized for following the prey while eloping from the initial position to the final position, which is attained by the equation (63), $H(e)$ is the current solution of e^{th} iteration.

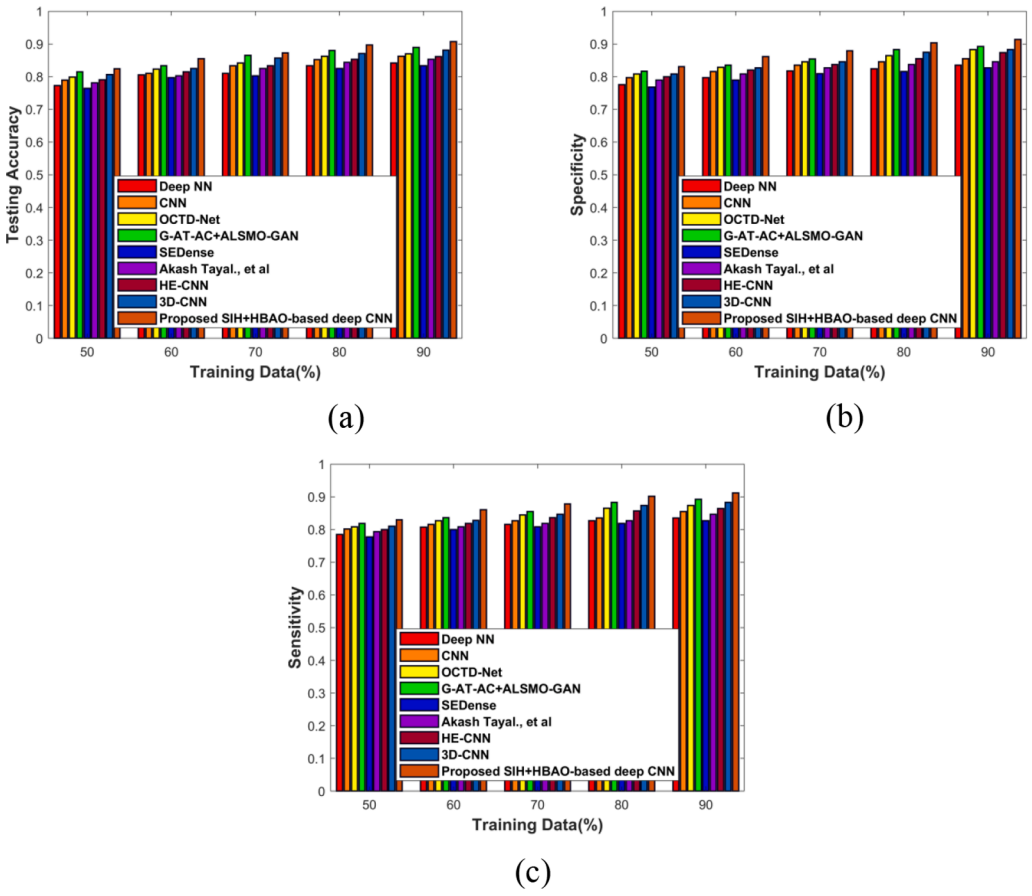

Fig. 7. Analysis based on 2nd level classification a) Testing accuracy, b) Specificity, c) Sensitivity.

$$Q_f(e) = e^{\frac{2\times rand(\,)-1}{(1-N)^2}} \tag{64}$$

$$\Im_1 = 2 \times rand(\,) - 1 \tag{65}$$

$$\Im_2 = 2 \times \left(1 - \frac{e}{N}\right) \tag{66}$$

The above equation (61), $Q_f(e)$ indicates the quality function value at e^{th} iteration.

Step 7: Termination

The top-mentioned steps are continuously done till an optimum solution is obtained.

3.5. DME classification utilizing proposed HBAO-Based deep CNN

If DME is detected as abnormal, then classification is performed, Here, DME is classified into retinal thickening, serious retinal detachment, cystoid macular, posterior hyloid traction, and tractional retinal detachment categories. The classification is performed by deep CNN that is tuned by the proposed HBAO. The deep CNN training utilizing the proposed HBAO is already expounded in section 3.4.2.

4. Results and discussion

This portion elucidates about outcomes and deliberations of the proposed SIH+HBAO-based deep CNN with respective measures of evaluation like accuracy, specificity and sensitivity. Moreover, experimentation setup, description of the database, evaluation measures and experimental outcomes, analysis based on performance as well as comparative techniques and comparative techniques discussion are described beneath.

4.1. Experimentation setup

An implementation of the proposed approach for the detection and classification of DME is executed in the MATLAB tool. Table 2 shows the experimental parameters of the proposed method.

4.2. Database description

The Optical Coherence Tomography Image Retinal Database (OCTIRD) database [35] comprises OCT images catalogued into various diseases and has high-resolution images in jpeg format, which could be downloaded as zip files. This database comprises more than 500 OCT volumetric scans of the spectral domain, comprising of four categories namely, Normal, Age-related Macular Degeneration, Macular Hole, Central Serous Retinopathy (CSR) and DR. Type of disease identified is Congenital muscular dystrophy (CMD), dentato-rubro-thalamic tract (DRT), Pulmonary hypertension (PHT), Sepiapterin reductase deficiency (SRD), and Treatment-resistant depression (TRD) based on classes.

Table 3 shows the types of diseases and total images of each disease.

4.3. Performance measures

The proposed technique for DME detection and classification is investigated for its performance using evaluation measures mentioned below in subsections.

4.3.1. Testing accuracy

Accuracy is defined as the closeness of the calibrated value to the known or standard value. It is formulated by,

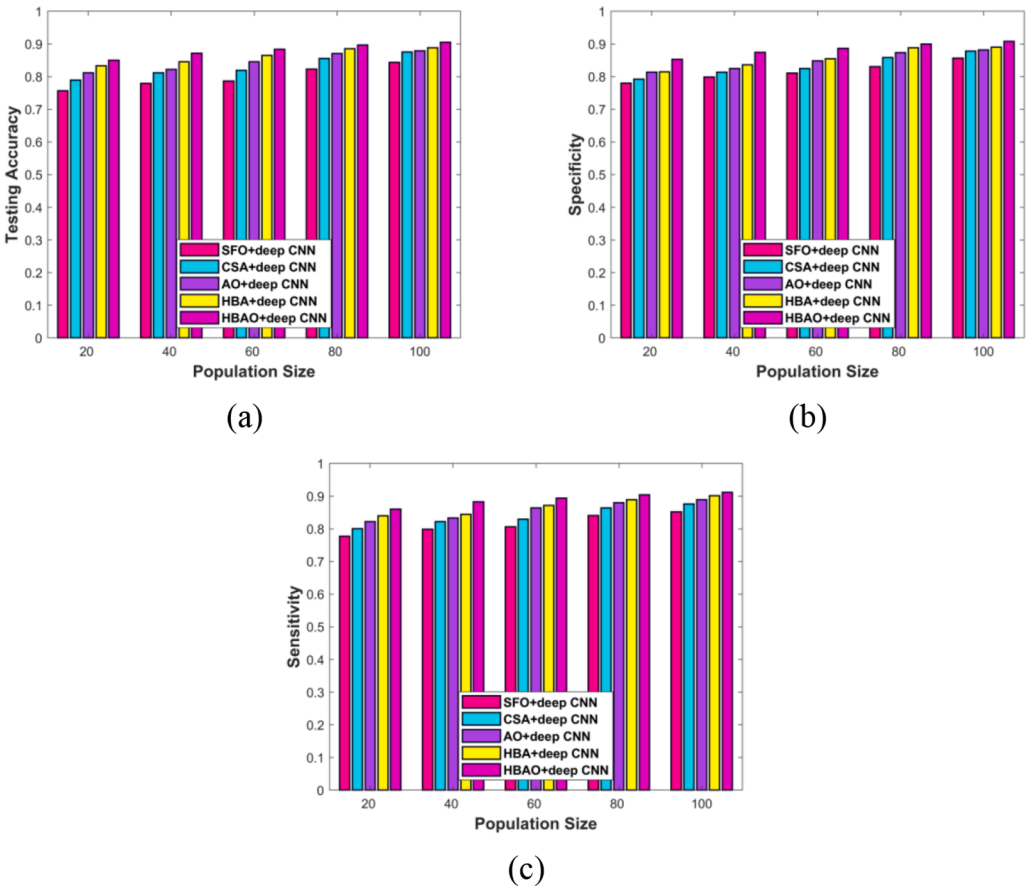

Fig. 8. An algorithm evaluation of the proposed algorithm by changing the population sizes a) Testing accuracy, b) Specificity, c) Sensitivity.

$$T_a = \frac{t_\rho + t_\eta}{t_\rho + t_\eta + f_\rho + f_\eta} \tag{67}$$

Here, t_ρ symbolizes true positive, t_η implies true negative. f_ρ Mentioned false positive and f_η false negative, correspondingly.

4.3.2. Sensitivity

It is a true positive rate signifies the possibility of positive test cases, conditioned on actually being positive and hence it is represented by,

$$S_e = \frac{t_\rho}{t_\rho + f_\eta} \tag{68}$$

4.3.3. Specificity

It is a true negative rate defined as the possibility of negative test cases, conditioned on actually being negative and is revealed by,

$$S_p = \frac{t_\eta}{t_\eta + f_\rho} \tag{69}$$

4.4. Experimental results

Experimentation outcomes of the proposed DME detection and classification approach are illustrated in Fig. 3. Fig. 3 a) delineates an input image-1and input image-2 is depicted in Fig. 3 b). Fig. 3 c) reveals the filtered image-1 whereas Fig. 3 d) portrays filtered image-2. Segmented image-1 is illustrated in Fig. 3 e) and Fig. 3 f) represents segmented image-2. Fig. 3 g) depicts an extracted image-1 of the LGP feature whereas Fig. 3 h) portrays an extracted image-2 of the LGP feature.

4.5. Performance analysis

This portion interprets an assessment of performance by the proposed SIH+HBAO-based deep CNN technique concerning 1st level classification (detection of DME) and 2nd level classification (classification of DME) level classifications with diverse epoch sizes.

4.5.1. Analysis based on 1st level classification

Fig. 4 illustrates an assessment of the proposed SIH+HBAO-based deep CNN by changing iterations from 50 to 250 with diverse epoch sizes. Performance analysis based upon testing accuracy by varying iterations with diverse epoch sizes is revealed in Fig. 4 a). When iteration = 50, the proposed SIH+HBAO-based deep CNN model with epoch size 100 is 0.839. A performance analysis based upon specificity by varying iterations with diverse epoch sizes is represented in Fig. 4 b). When iteration = 50, the performance analysis of specificity for the proposed model with epoch size 100 is 0.833. Fig. 4 c) shows the performance analysis based on sensitivity by varying iterations with different epoch sizes. For iteration = 50, the sensitivity for the proposed model with epoch size 20 is 0.785.

4.5.2. Analysis based on 2nd level classification

Fig. 5 elucidates an assessment of the proposed SIH+HBAO-based deep CNN by changing iterations from 50 to 250 with diverse epoch sizes. Performance analysis based upon testing accuracy by varying iterations with diverse epoch sizes is shown in Fig. 5 a). When iteration = 50, the performance analysis of testing accuracy for the proposed SIH+HBAO-based deep CNN model with epoch size 100 is 0.835. Fig. 5 b) reveals the performance evaluation of the proposed SIH+HBAO-based deep CNN based upon specificity by varying iterations with different epoch sizes. While iteration = 50, the performance analysis of

specificity for the proposed model with epoch size is 0.827. Fig. 5(c) shows the performance analysis based on sensitivity by varying iterations with diverse epoch sizes. For iteration = 50, the performance analysis of sensitivity for the proposed model with epoch size 100 is 0.834.

4.6. Comparative techniques

The current techniques like Deep NN [1], CNN [2], OCTD-Net [3], G-AT-AC+ALSMO-GAN, SEDense [44], and Akash Tayal., et al. [7], HE-CNN [49], and 3D-CNN [50] are examined with the proposed SIH+HBAO-based deep CNN to prove the effectiveness of the proposed model.

4.7. Comparative analysis

This section describes a comparison assessment of the proposed SIH+HBAO-based deep CNN concerning evaluation measures by altering a percentage of training data.

4.7.1. Analysis based upon 1st level classification

The comparison evaluation of the proposed SIH+HBAO-based deep CNN based on 1st-level classification considering evaluation measures is revealed in Fig. 6. An evaluation of the proposed SIH+HBAO-based deep CNN with respective to testing accuracy is interpreted in Fig. 6 a). A testing accuracy achieved by the proposed method is 0.912 whereas other techniques like Deep NN, CNN, OCTD-Net, G-AT-AC+ALSMO-GAN, SEDense, Akash Tayal., *et al,* HE-CNN, and 3D-CNN attained the values of 0.847, 0.867, 0.885, 0.895, 0.839, 0.858, 0.876, and 0.886 for 90% of training data. Fig. 6 b) interprets an estimation of the proposed SIH+HBAO-based deep CNN regarding specificity. The specificity achieved by SIH+HBAO-based deep CNN is 0.918 whereas other techniques Deep NN, CNN, OCTD-Net, G-AT-AC+ALSMO-GAN, SEDense, Akash Tayal., *et al,* HE-CNN, and 3D-CNN attained 0.847, 0.866, 0.894, 0.904, 0.838, 0.858,0.885, and 0.895 for 90% of training data. An evaluation of the proposed SIH+HBAO-based deep CNN with respective sensitivity is delineated in Fig. 6 c). The sensitivity acquired by the proposed SIH+HBAO-based deep CNN is 0.917 whereas the other techniques Deep NN, CNN, OCTD-Net, G-AT-AC+ALSMO-GAN, SEDense, Akash Tayal., *et al,* HE-CNN, and 3D-CNN achieved 0.847, 0.867, 0.894, 0.904, 0.904, 0.839, 0.858, and 0.886 for 90% of training data.

4.7.2. Analysis based upon 2nd level classification

Fig. 7 elucidates the comparison assessment of the proposed SIH+HBAO-based deep CNN based upon the 2nd-level classification. Fig. 7 a) reveals an estimation of the proposed SIH+HBAO-based deep CNN with respective to testing accuracy. From the figure, it is observed that the testing accuracy attained by the proposed SIH+HBAO-based deep CNN is 0.907 whereas other techniques like Deep NN, CNN, OCTD-Net, G-AT-AC+ALSMO-GAN, SEDense, Akash Tayal., *et al.* HE-CNN, and 3D-CNN attained 0.842, 0.862, 0.870, 0.890, 0.834, 0.853, 0.861, and 0.881 for 90% of data. An estimation of the proposed SIH+HBAO-based deep CNN with respective specificity is shown in Fig. 7 b). The specificity achieved by the proposed SIH+HBAO-based deep CNN is 0.913 whereas other techniques Deep NN, CNN, OCTD-Net, G-AT-AC+ALSMO-GAN, SEDense, Akash Tayal., *et al.* HE-CNN, and 3D-CNN achieved 0.835, 0.854, 0.882, 0.892, 0.827, 0.846, 0.874 and 0.883 for 90% of training data. Fig. 7 c) reveals an estimation of the proposed SIH+HBAO-based deep CNN with respective sensitivity. The sensitivity attained by SIH+HBAO-based deep CNN is 0.912 whereas the other techniques Deep NN, CNN, OCTD-Net, G-AT-AC+ALSMO-GAN, SEDense, Akash Tayal., *et al.* HE-CNN, and 3D-CNN obtained 0.835, 0.855, 0.873, 0.892, 0.827, 0.847, 0.864, and 0.883 for 90% of the training data.

4.8. Algorithmic analysis

The several algorithms taken for evaluation include, Sail Fish Optimizer (SFO) [30]+deep CNN, Crow Search Algorithm CSA [31] +deep CNN, AO +deep CNN and HBA +deep CNN. Furthermore, an algorithmic evaluation is carried out concerning evaluation measures by

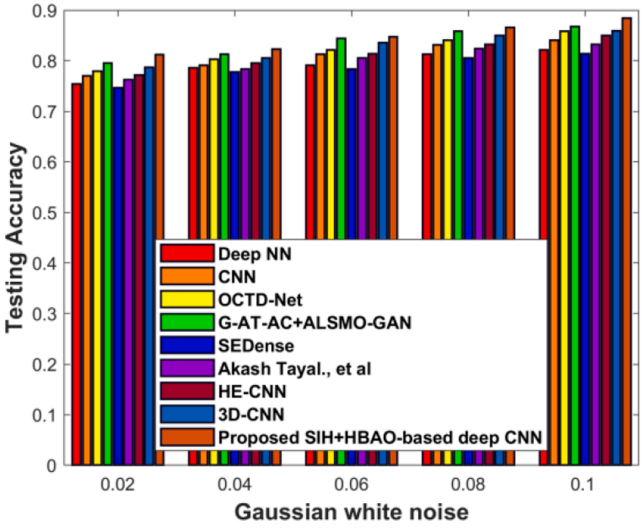

Fig. 10. Analysis of the proposed model in a noisy environment.

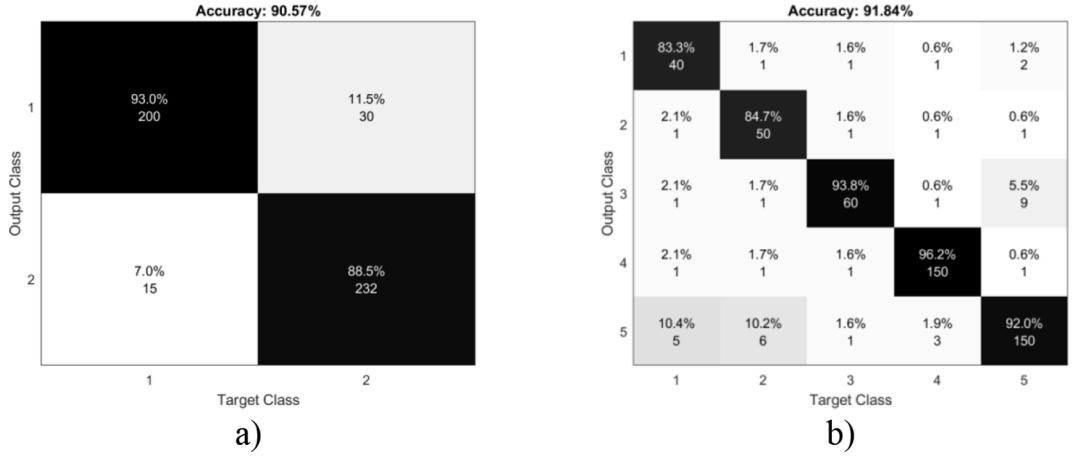

Fig. 9. Confusion matrix for a) 1st classification, and b) 2nd classification.

Table 4
Comparative discussion of SIH+HBAO-based deep CNN.

Training g data = 90%	Classifications	Metrics/ Methods	Deep NN	CNN	OCTD-Net	G-AT-AC+ALSMO-GAN	SEDense	Akash Tayal., *et al*	HE-CNN	3D-CNN	Proposed SIH+HBAO-based deep CNN
	1st levelclassification	Accuracy (%)	0.847	0.867	0.885	0.895	0.839	0.858	0.876	0.886	0.912
		Specificity (%)	0.847	0.866	0.894	0.904	0.838	0.858	0.885	0.895	0.918
		Sensitivity (%)	0.847	0.867	0.894	0.904	0.839	0.858	0.886	0.895	0.917
	2nd levelclassification	Accuracy (%)	0.842	0.862	0.870	0.890	0.834	0.853	0.861	0.881	0.907
		Specificity (%)	0.835	0.854	0.882	0.892	0.827	0.846	0.874	0.883	0.913
		Sensitivity (%)	0.835	0.855	0.873	0.892	0.827	0.847	0.864	0.883	0.912

varying population sizes from 20-100.

Fig. 8 represents the algorithmic estimation of the proposed algorithm with respective performance measures by altering the population sizes. An evaluation utilizing testing accuracy is shown in Fig. 8 a). When the population size is 100, the testing accuracy attained by HBA+deep CNN is 0.905. An assessment using specificity is delineated in Fig. 8 b). When the population size is 100, the specificity achieved by HBA +deep CNN is 0.908 whereas other algorithms such as SFO +deep CNN, CSA +deep CNN, AO +deep CNN and HBA +deep CNN achieved 0.857, 0.878, 0.882 and 0.891. An evaluation utilizing sensitivity is illustrated in Fig. 8 c). The sensitivity attained by HBA +deep CNN is 0.912 whereas the existing approaches acquired 0.852, 0.876, 0.889 and 0.901 when the population size is 100.

4.9. Confusion matrix

Fig. 9 represents the confusion matrix for the 1st and 2nd classifications. A table called a confusion matrix is used to assess the performance of a classification algorithm. A confusion matrix is used to display and summarize a classification algorithm's performance.

4.10. Analysis of the proposed model in a noisy environment

Fig. 10 shows the analysis of the proposed model in a noisy environment. Multi-modal optimization algorithms in noise environments are of great significance. When the Gaussian white noise is 0.1, the testing accuracy obtained by the proposed SIH+HBAO-based deep CNN is 0.884 whereas other techniques Deep NN, CNN, OCTD-Net, G-AT AC+ALSMO-GAN, SEDense, Akash Tayal., et al, HE-CNN, and 3D-CNN achieved 0.822, 0.841, 0.858, 0.868, 0.814, 0.833, 0.850, and 0.859, respectively. The proposed method provided a more accurate location of the optimum point and more local extreme points in a noisy environment. So, the Proposed SIH+HBAO-based deep CNN method is better for noisy environments than the existing methods.

4.11. Comparative discussion

The comparative discussion of the newly introduced SIH+HBAO-based deep CNN is shown in Table 4. Using 1st level classification, the supreme accuracy of 91.2 %, the sensitivity of 91.7 %, and specificity of 91.8 % are observed by SIH+HBAO-based deep CNN by altering training data 90 %. Concerning 2nd level classification, the augmented accuracy of 90.7 %, the sensitivity of 91.2 %, and the specificity of 91.3 % are noted by SIH+HBAO-based deep CNN when considering 90 % of training data. Besides, by combining the HBA, and the AO algorithm, the devised SIH+HBAO algorithm achieved enhanced exploration and exploitation capabilities and minimised the training speed.

5. Conclusion

DME is developed in diabetic patients with an enhancement of DR. It is formed by fluid accumulation in the macula, which directs to impairment of vision or blindness. Therefore, earlier detection and classification would assist ophthalmologists in protecting DME patients in a perfect manner. This paper proposed a proficient detection and classification technique for DME based on the proposed SIH+HBAO-based deep CNN. Firstly, the input image is considered from a particular dataset followed by pre-processing is done utilizing a Gaussian filter. Then, layer segmentation is done by Correlative-based gradient global thresholding with active contour. After, layer segmentation, extraction of features is carried out. Additionally, texture features like LGP and proposed SIH with multi-kernel are extracted. The proposed SIH with the multi-kernel feature is designed by modifying the shape index histogram with multi-kernel. Finally, DME 1st level and 2nd level classification is conducted utilizing Deep CNN, which is trained to employ the HBAO algorithm. In 1st level classification, DME is classified as normal or abnormal cases whereas 2nd level, the abnormal cases are further classified employing Deep CNN, which is tuned using the HBAO algorithm. The proposed HBAO algorithm is devised by a combination of HBA and AO. Moreover, the SIH+HBAO-based deep CNN has acquired a maximal accuracy of 0.912, sensitivity of 0.913 and specificity of 0.917 for 1st-level classification when considering 90 % of training data. Future research will concentrate on the combination of DR and DME problems in order to improve DME identification and classification.

CRediT authorship contribution statement

Shweta Reddy: Visualization, Writing – original draft, Writing – review & editing. **Shridevi Soma:** Supervision, Validation.

Declaration of competing interest

The authors declare that they have no known competing financial interests or personal relationships that could have appeared to influence the work reported in this paper.

Data availability

No data was used for the research described in the article.

References

[1] H.S. Sandhu, A. Eltanboly, A. Shalaby, R.S. Keynton, S. Schaal, A. El-Baz, Automated diagnosis and grading of diabetic retinopathy using optical coherence tomography, Invest. Ophthalmol. Vis. Sci. 59 (7) (2018) 3155–3160.
[2] M. Ghazal, S.S. Ali, A.H. Mahmoud, A.M. Shalaby, A. El-Baz, Accurate detection of non-proliferative diabetic retinopathy in optical coherence tomography images using convolutional neural networks, IEEE Access 8 (2020) 34387–34397.
[3] X. Li, L. Shen, M. Shen, F. Tan, C.S. Qiu, Deep learning based early stage diabetic retinopathy detection using optical coherence tomography, Neurocomputing 369 (2019) 134–144.
[4] Rajeev Kumar Singh, Rohan Gorantla, "DMENet: diabetic macular edema diagnosis using a hierarchical ensemble of CNNs", Plos one, vol.15, no.2, pp.e0220677, 2020.
[5] S. Vellakani, I. Pushbam, An enhanced OCT image captioning system to assist ophthalmologists in detecting and classifying eye diseases, J. Xray Sci. Technol. 28 (5) (2020) 975–988.
[6] X. Li, Hu. Xiaowei, Yu. Lequan, L. Zhu, Fu. Chi-Wing, P.-A. Heng, CANet: cross-disease attention network for joint diabetic retinopathy and diabetic macular edema grading, IEEE Trans. Med. Imaging 39 (5) (2019) 1483–1493.

[7] A. Tayal, J. Gupta, A. Solanki, K. Bisht, A. Nayyar, M. Masud, DL-CNN-based approach with image processing techniques for the diagnosis of retinal diseases, Multimedia Syst. (2021) 1–22.
[8] Joaquim de Moura, Gabriela Samagaio, Jorge Novo, Pablo Almuina, Maŕıa Isabel Fernandez, Marcos Ortega, "Joint diabetic macular edema segmentation and characterization in OCT images", Journal of Digital Imaging, vol.33, no.5, pp.1335-1351, 2020.
[9] J.M. Schmitt, Optical coherence tomography (OCT): a review, IEEE J. Sel. Top. Quantum Electron. 5 (4) (1999) 1205–1215.
[10] D. Huang, E.A. Swanson, C.P. Lin, J.S. Schuman, W.G. Stinson, W. Chang, M. R. Hee, T. Flotte, K. Gregory, C.A. Puliafito, J.G. Fujimoto, Optical Coherence Tomography Science 254 (5035) (1991) 1178–1181.
[11] Khaled Alsaih, Guillaume Lemaıtre, Join Massich Vall, Mojdeh Rastgoo, Desire Sidibe, Tien Y Wong, Ecosse Lamoureux, Dan Milea, Carol Y Cheung and Fabrice Meriaudeau, "Classification of SD-OCT volumes with multi pyramids, LBP and HOG descriptors: application to DME detections", In proceedings of 38th Annual international conference of the IEEE engineering in medicine and biology society (EMBC), pp. 1344-1347, 2016.
[12] Gabriele E. Lang, "Diabetic macular edema", Ophthalmologica, vol.227, pp.21-29, 2012.
[13] Francesco Bandello, Maurizio Battaglia Parodi, Paolo Lanzetta, Anat Loewenstein, Pascale Massin, Francesca Menchini and Daniele Veritti, "Diabetic macular edema", Macular Edema, vol.47, pp.73-110, 2010.
[14] A. Rainer, Leitgeb and Bernhard Baumann "Multimodal optical medical imaging concepts based on optical coherence tomography", Front. Phys. 6 (2018) 114.
[15] Y. Rao, N.P. Dr, Sarwade and Roshan Makkar "Modeling and simulation of optical coherence tomography on virtual OCT", Procedia Comput. Sci. 45 (2015) 644–650.
[16] Pin-Hsien Lee, Pin-Hsien Lee, Sheng-Lung Huang, Andrew Chen and Homer H. Chen, "Blood vessel extraction from OCT data by short-time RPCA", In Proceedings of IEEE International Conference on Image Processing (ICIP), pp. 394-398, 2016.
[17] R. Benarous, M.B. Sasongko, S. Qureshi, E. Fenwick, M. Dirani, T.Y. Wong, E. L. Lamoureux, Differential association of serum lipids with diabetic retinopathy and diabetic macular edema, Invest. Ophthalmol. Vis. Sci. 52 (10) (2011) 7464–7469.
[18] Eun Jee Chung, Mi In Roh, Oh Woong Kwon, Hyoung Jun Koh, "Effects of macular ischemia on the outcome of intravitreal bevacizumab therapy for diabetic macular edema", Retina, vol.28, no.7, pp.957-963, 2008.
[19] P.A. Campochiaro, Reduction of diabetic macular edema by oral administration of the kinase inhibitor PKC412, Invest. Ophthalmol. Vis. Sci. 45 (3) (2004) 922–931.
[20] F. Bandello, D. Roman Pognuz, A. Polito, A. Pirracchio, F. Menchini and M. Ambesi, "Diabetic macular edema: classification, medical and laser therapy", In Seminars in ophthalmology (Taylor & Francis), vol.18, no.4, pp. 251-258, 2003.
[21] T. Daghistani, Using Artificial Intelligence for Analyzing Retinal Images (OCT) in People with Diabetes: Detecting Diabetic Macular Edema Using Deep Learning Approach, Transactions 10 (1) (2022) 41–49.
[22] S.K. Somasundaram, P. Alli, A machine learning ensemble classifier for early prediction of diabetic retinopathy, J. Med. Syst. 41 (12) (2017) 1–12.
[23] S.S. Yadav, S.M. Jadhav, Deep convolutional neural network based medical image classification for disease diagnosis, Journal of Big Data 6 (1) (2019) 1–18.
[24] F. Ren, P. Cao, D. Zhao, C. Wan, Diabetic macular edema grading in retinal images using vector quantization and semi-supervised learning, Technol. Health Care 26 (S1) (2018) 389–397.
[25] Adeel M. Syed, M. Usman Akram, Tahir Akram, Muhammad Muzammal, Shehzad Khalid and Muazzam Ahmed Khan, "Fundus images-based detection and grading of macular edema using robust macula localization", IEEE Access, vol.6, pp.58784-58793, 2018.
[26] C. Bhardwaj, S. Jain, M. Sood, Deep learning–based diabetic retinopathy severity grading system employing quadrant ensemble model, J. Digit. Imaging 34 (2) (2021) 440–457.
[27] G. Deng and L. W. Cahill, "An adaptive Gaussian filter for noise reduction and edge detection", In Proceedings of IEEE Conference record nuclear science symposium and medical imaging conference, pp. 1615-1619, 1993.
[28] H. Yazid, H. Arof, Gradient-based adaptive thresholding, J. Vis. Commun. Image Represent. 24 (7) (2013) 926–936.
[29] Ashutosh Kumar Chaubey, Comparison of the local and global thresholding methods in image segmentation, World Journal of Research and Review 2 (1) (2016) 1–4.
[30] S. Shadravan, H.R. Naji, V.K. Bardsiri, The Sailfish Optimizer: A novel nature-inspired metaheuristic algorithm for solving constrained engineering optimization problems, Eng. Appl. Artif. Intel. 80 (2019) 20–34.
[31] A. Askarzadeh, A novel metaheuristic method for solving constrained engineering optimization problems: crow search algorithm, Comput. Struct. 169 (2016) 1–12.
[32] Anders Boesen Lindbo Larsen, Jacob Schack Vestergaard and Rasmus Larsen, "HEp-2 cell classification using shape index histograms with donut-shaped spatial pooling", IEEE Trans. Med. Imag., vol.33, no.7, pp.1573-1580, 2014.
[33] Laith Abualigah, Dalia Yousri, Mohamed Abd Elaziz, Ahmed A. Ewees, Mohammed A. A. Al-qaness and Amir H. Gandomi, "Aquila optimizer: a novel meta-heuristic optimization algorithm", Computers & Industrial Engineering, vol.157, pp.107250, 2021.
[34] F.A. Hashim, F.A. Hashim, K. Hussain, M.S. Mabrouk, W. Al-Atabany, Honey Badger Algorithm: New metaheuristic algorithm for solving optimization problems, Math. Comput. Simul 192 (2022) 84–110.
[35] Optical Coherence Tomography Image Retinal Database, "https://www.openicpsr.org/openicpsr/project/108503/version/V1/view", accessed on June 2022.
[36] Fengbin Tu, Shouyi Yin, Peng Ouyang, Shibin Tang, Leibo Liu, Shaojun Wei, "Deep convolutional neural network architecture with reconfigurable computation patterns", IEEE Transactions on Very Large Scale Integration (VLSI) Systems, vol.25, no.8, pp.2220-2233, 2017.
[37] Ninu Preetha and Praveena S, "Multiple Feature Sets and SVM Classifier for the Detection of Diabetic Retinopathy Using Retinal Images", Multimedia Research, vol.1, no.1, pp.17-26, 2018.
[38] Arun T Nair, Muthuvel K., "Diabetic Retinopathy Recognition using Enhanced Crow Search with Levy Flight Algorithm", Multimedia Research, vol.2, no.4, pp.43-52, 2019.
[39] Plácido L. Vidal, Joaquim de Moura, Macarena Díaz, Jorge Novo, and Marcos Ortega, "Diabetic Macular Edema Characterization and Visualization Using Optical Coherence Tomography Images", Applied Sciences, vol.10, no.21, 2020.
[40] X. Liu, S. Wang, Y. Zhang, D. Liu, Hu. Wei, Automatic fluid segmentation in retinal optical coherence tomography images using attention-based deep learning, Neurocomputing 452 (2021) 576–591.
[41] Dr Puspita Dash, A.N. Sigappi, "Detection and recognition of diabetic macular edema from oct images based on local feature descriptor", International Journal of Pure and Applied Mathematics, vol.119, no.14, pp.1-7, 2018.
[42] Amit Kumar, Anand Shanker Tewari, Jyoti Prakash Singh, "Classification of diabetic macular edema severity using deep learning technique", Research on Biomedical Engineering, vol.38, pp.977-987, 2022.
[43] Amit Kumar, and Anand Shanker Tewari, "Risk Identification of Diabetic Macular Edema Using E-Adoption of Emerging Technology", International Journal of E-Adoption (IJEA), vol.14, no.3, pp.1-20,2022.
[44] Amit Kumar, Anand Shanker Tewari, Classifying diabetic macular edema grades using extended power of deep learning, Multimedia Tools Applications, 2023.
[45] Walaa N. Ismail, Hessah A. Alsalamah, Efficient Harris Hawk Optimization (HHO)-Based Framework for Accurate Skin Cancer Prediction, "Health and Medicine., vol.11, no.16, August 2023.
[46] Walaa N. Ismail, Hessah A. Alsalamah, Mohammad Mehedi Hassan, Ebtesam Mohamed., "AUTO-HAR: An adaptive human activity recognition framework using an automated CNN architecture design", Heliyon, vol.9, no.2, February 2023.
[47] Hongbiao Zhou, Yu Zhang, Weiping Duan, Huanyu Zhao., Nonlinear systems modelling based on a self-organizing fuzzy neural network with hierarchical pruning scheme, Appl. Soft Comput., vol. 95, October 2020.
[48] Hongbiao Zhou, Yang Li, Qinyu Zhang, Haoyuan Xu, and Yan Su., "Soft-sensing of effluent total phosphorus using an adaptive recurrent fuzzy neural network with Gustafson-Kessel clustering", Expert Systems with Applications, vol. 203, October 2022.
[49] Rajeev Kumar Singh, Rohan Gorantla, DMENet: diabetic macular edema diagnosis using hierarchical ensemble of CNNs", vol. 15, no. 2, February 2020.
[50] Xiuping Han, Juan Tan, Yumei He, Deep learning algorithm-based MRI image in the diagnosis of diabetic macular edema", vol.2022, Mar 2022.
[51] Zeru Hai, Beiji Zou, Xiaoxia Xiao, Qinghua Peng, Junfeng Yan, Wensheng Zhang, Kejuan Yue, A novel approach for intelligent diagnosis and grading of diabetic retinopathy, Comput. Biol. Med., vol. 172, April 2024.